polysaccharides

MDPI

Article

Use of a Hybrid Porous Carbon Material Derived from Expired Polysaccharides Snack/Iron Salt Exhibiting Magnetic Properties, for Hexavalent Chromium Removal

Maria Baikousi [1,*], Konstantinos Moustaklis [1], Angeliki Karakassides [1], Georgios Asimakopoulos [1], Dimitrios Moschovas [1], Apostolos Avgeropoulos [1], Athanasios B. Bourlinos [2], Alexios P. Douvalis [2], Constantinos E. Salmas [1,*] and Michael A. Karakassides [1]

[1] Department of Materials Science & Engineering, University of Ioannina, 45110 Ioannina, Greece; ntinos.mous4624@gmail.com (K.M.); akarakasidou1@gmail.com (A.K.); asimakopoulos.geo@gmail.com (G.A.); dmoschov@uoi.gr (D.M.); aavger@uoi.gr (A.A.); mkarakas@uoi.gr (M.A.K.)

[2] Physics Department, University of Ioannina, 45110 Ioannina, Greece; bourlino@uoi.gr (A.B.B.); adouval@uoi.gr (A.P.D.)

* Correspondence: mbaikou@uoi.gr (M.B.); ksalmas@uoi.gr (C.E.S.); Tel.: +30-26510-07412 (M.B.); +30-26510-07253 (C.E.S.)

check for updates

Citation: Baikousi, M.; Moustaklis, K.; Karakassides, A.; Asimakopoulos, G.; Moschovas, D.; Avgeropoulos, A.; Bourlinos, A.B.; Douvalis, A.P.; Salmas, C.E.; Karakassides, M.A. Use of a Hybrid Porous Carbon Material Derived from Expired Polysaccharides Snack/Iron Salt Exhibiting Magnetic Properties, for Hexavalent Chromium Removal. *Polysaccharides* **2022**, *3*, 326–346. https://doi.org/10.3390/polysaccharides3020019

Academic Editors: Cédric Delattre and Alessandra Braga Ribeiro

Received: 27 December 2021
Accepted: 1 April 2022
Published: 5 April 2022

Abstract: Nowadays, the scientific interest is focused more and more on the development of new strategies in recycling of waste products as well as on the development of clean technologies due to the increased environmental pollution. In this work we studied the valorization of an expired cheese-tomato flavor corn snack, which is polysaccharide food product, by producing advanced hybrid magnetic materials for environmental remediation purposes. The carbonization-chemical activation of this snack using potassium hydroxide leads to a microporous activated carbon with high surface area (S_{gBET} ~800 m^2/g). The magnetic hybrid material was synthesized via an in-situ technique using iron acetate complex as the precursor to produce iron based magnetic nanoparticles. The resulting material retains a fraction of the microporous structure with surface area S_{gBET} ~500 m^2/g. Such material consists, of homogenously dispersed magnetic isolated zero valent iron nanoparticles and of iron carbides (Fe_3C), into the carbon matrix. The magnetic carbon exhibited high adsorption capacity in Cr(VI) removal applications following a pseudosecond order kinetic model. The maximum adsorption capacity was 88.382 $mg_{Cr(VI)}/g_{AC}$ at pH = 3. Finally, oxidation experiments, in combination with FT-IR, Mössbauer, and VSM measurements indicated that the possible Cr^{6+} removal mechanism involves oxidation of iron phases and reduction of Cr^{6+} to Cr^{3+}.

Keywords: potassium hydroxide activation; zero valent iron; iron carbides; magnetic nanoparticles; kinetic study; hexavalent chromium; cheese-tomato flavor corn snack

1. Introduction

In the recent years, following the trend to minimize the landfilled waste products and to valorize several biomass byproducts various recycling strategies have been tested. One of the most promising is the production of porous carbon materials for different applications such as water purification, catalysis, energy storage and gas adsorption [1–4]. In the EU28, approximately 88 million tons of foods which costs €143 billion are wasted annually [5,6]. Many products in the food industry such as cereal foods, cornmeal, pretzels, flours, oats, pasta, rice, potato, corn, roots, fruits, seeds, vegetables, etc. consist of polysaccharides such as starch, maltodextrin, glycogen, cellulose, pectin, amylose, amylopectin, etc. and other mono-, di- or oligo- saccharides such as sucrose, glucose, fructose, etc. [7,8]. Such molecules can act as carbon sources for the production of porous carbon materials by using different synthetic approaches such as pyrolysis with chemical, physical, or catalytic activation, polymerization and carbonization, template methods etc. [9].

Activated carbons are the high surface area porous carbon materials, which are produced by chemical or physical activation of char. Chemical activation is carried out using an activating agent like KOH, $KHCO_3$, K_2CO_3, $ZnCl_2$, $CaCl_2$ H_2SO_4, H_3PO_4 and CO_2 [10]. These materials are considered among the most widely used absorbents for environmental remediation applications due to their low cost, high porosity, tunable pore size and high adsorption capacities [11]. Cr(VI) is a highly soluble heavy metal that exerts toxic effects on humans and animals [12,13]. However, it is produced in many industrial processes, resulting in concentration of 0.5–270 mg/L Cr(VI) in industrial wastewaters which is much more higher than the permissible level for living organisms (0.05 mg/L) according to the WHO (World Health Organization) [14–16]. Therefore, it is of vital importance the finding of new materials and techniques for water purification from hexavalent chromium. Among the different methods that have been proposed for Cr(VI) removal (chemical precipitation, ion exchange, membrane filtration, electrochemical treatment and adsorption), adsorption seems to be one of the most preferable methods due to its high efficiency, simplicity and low cost [13,17–19]. As it is reported in literature, various biomass sources have been used following the cyclic economy spirit, to synthesize activated carbon for the removal of the toxic hexavalent chromium. Mango kernel [20], coconut tree sawdust [21], coconut shell [22], bael fruit shell [23], peanut shell [17], "Posidonia oceanica" [24], etc. [25–29] are some kinds of biomass that have been used for this purpose.

Furthermore, iron based magnetic nanoparticles attracted significant attention from the scientific community for Cr(VI) removal applications, due to their simple and low cost production, small particle size, and high surface area and catalytic activity, as they compared to other corresponding bulk materials [30–33]. However, such kind of nanoparticles, are easily oxidized in air and trend to agglomerate, decreasing their efficiency in heavy metal adsorption/reduction process. The combination of a porous carbon with iron magnetic nanoparticles can overcome these difficulties, leading to hybrid materials. Such materials composed with protected and isolated magnetic nanoparticles into the carbon matrix exhibiting advanced sorption properties for environmental remediation [34–36]. The porous carbon materials act as effective supports due to their high specific surface area and resistance to acidic and basic conditions. Also their surface can be functionalized to provide controlled metal loading sites [37]. Such carbon/iron composites exhibit enchanced efficiency for environmental applicatons derived from both the higher reactivity of the iron nanoparticles and simultaneously the active role of the porous carbon matrix in the catalytic and sorption processes [38].

In this work we present the possibility to use an expired food product, a cheese-tomato flavor corn snack, for the synthesis of a hybrid magnetic carbon material for the first time. Also we investigate its effectiveness in environmental applications such as for hexavalent chromium removal from aqueous solutions. This snack contains several polysaccharides which can be carbonized and activated for the production of an activated carbon with high surface area. The combination of Fe^{3+} ions with acetic acid vapors during the activation process leads to an advanced magnetic hybrid material. This low cost and one step carbonization aproach leads to the formation of isolated zero valent iron nanoparticles on a carbon matrix, with high effectiveness in hexavalent chromium removal applications. A post-treatment method but with a different carbon matrix has been previously reported by our team [39] for the production of magnetic hybrid material. According to this literature, even the produced hybrid material shown higher surface area, it consisted of lower content of magnetic nanoparticles and also exhibited lower effectiveness in hexavalent chromium sorption process.

2. Materials and Methods

2.1. Materials and Chemical Reagents

Expired cheese-tomato flavor corn snack (Cheetos, here it is defined as "snack") was supplied from the local market. According to the package information, the snack contains the following ingredients: corn meal (55%), corn oil, potato granules, wheat flour, cheese

powder (4.1%), tomato powder (3.4%), rice flour, onion powder, salt, rusk powder, skimmed milk powder, lactose powder, sugar, dextrose, flavourings, yeast powder, acidity regulator (sodium acetates, citric acid), disodium 5′ ribonucleotide, rapeseed oil, celery seed, barley malt flour, smoke flavourings, spice, maltodextrin, paprika extract, sunflower oil, paprika powder. All the purchased chemical reagents were used in this work as received without further purification. More specific, iron(iii) nitrate nonahydrate ($Fe(NO_3)\cdot 9H_2O$), 1,5-diphenylcarbazide ($C_{13}H_{14}N_4O$, ≥97%), potassium dichromate ($K_2Cr_2O_7$, 99.98%), hydrochloric acid (HCl, 37%), acetic acid (99.5%), acetone (99.9%)and phosphoric acid (H_3PO_4, 85%) were purchased from Merck (Merck, Darmstadt, Germany), potassium hydroxide (KOH, 85%) from Riedel-de Haen (Riedel-de Haen, Seelze, Germany) whereas ethanol 99.5% (EtOH) and methanol 99.8% (MeOH) from Panreac (Panreac, Barcelona, Spain).

2.2. Synthesis of Materials

2.2.1. Synthesis of AC-Snack

For the synthesis of bare activated carbon (AC) derived from the snack, without magnetic nanoparticles, 3 g of snack species were grounded and mixed with 3 g of activating agent KOH. The mixture was pyrolyzed for 30 min, under flowing Ar atmosphere, at 600 °C, with 10 °C/min increasing temperature rate. Then the produced carbon was washed with deionized water to remove the inorganic byproducts. The material was dried in room temperature under vacuum and the code name of the sample was AC-snack.

2.2.2. Synthesis of mAC-Snack

For the synthesis of the magnetic hybrid material, the following in-situ strategy was followed. Snack species (3 g) were impregnated with 60 mL iron nitrate solution (3 g of $Fe(NO_3)_3\cdot 9H_2O$, 10 mL MeOH), dried for 1 h at 80 °C and exposed to acetic acid vapors at 80 °C for 1 h. The produced snack/iron acetate species were dried for 30 min at 80 °C and continiously grounded and mixed with the activating agent 3 g KOH (weight ratio snack:KOH = 1:1). Finally, the powdered mixture snack/iron acetate/KOH was pyrolyzed for 30 min in Ar flowing atmosphere at 600 °C with 10 °C/min increasing temperature rate, washed with a 30/70 v/v H_2O/MeOH solution and dried in room temperature under vacuum (the code name of the sample is mAC-snack). A post-treatment method that have been previously reported by our team in different carbon matrix [39] was also tested for the production of magnetic hybrid material using the acticvated carbon derived from this snack (mAC-snack (p.t.)).

2.3. Characterization of Materials

The X-ray powder diffraction patterns of the materials were provided by a D8 Advance Bruker diffractometer (Bruker, Billerica, MA, USA) using Cu Ka (40 kV, 40 mA, λ = 1.541 78 Å) radiation and a secondary beam graphite monochromator (Measurement conditions: 2θ = 10–70 degrees, in steps of 0.02 degrees and 2 s counting time per step).

Infrared (FT-IR) spectroscopy was performed on powdered samples dispersed in KBr pellets using a JASCO FT/IR-6000, Fourier transform spectrometer (JASCO, Easton, PA, USA). The spectra are the average of 32 scans at 4 cm^{-1} resolution and were measured in the frequency range of 400–4000 cm^{-1}.

For the thermogravimetric (TGA) and differential thermal analysis (DTA) data, about 5 mg of the sample were heated in the air from 25 °C to 750 °C, with an increasing temperature rate of 5 °C/min using a Perkin Elmer Pyris Diamond TG/DTA instrument (Perkin Elmer, MA, USA).

The ^{57}Fe Mössbauer spectra of the magnetic material mAC-snack before and after the sorption experiments were collected in transmission geometry at room temperature (RT, 300 K) and 77 K, using constant-acceleration spectrometers (Wissel Elektronik GMBH, Starnberg, Germany), equipped with ^{57}Co(Rh) sources kept at RT and a liquid N_2 bath cryostat (Oxford Instruments, Witney-Oxon, England-UK). Velocity calibration of the spectrometers was carried out using metallic α-Fe at RT and all isomer shift (IS) values

are given relative to this standard. The experimentally recorded spectrum was fitted and analyzed using the IMSG code [40].

The magnetic properties of the magnetic material mAC-snack before and after the sorption experiments were investigated by means of isothermal magnetization (M) versus (vs.) applied magnetic field (H) measurements, which were conducted at room temperature using a vibrating sample magnetometer (VSM, LakeShore 7300, Westerville, OH, USA)

Transmission electron microscopy (TEM) observations were performed using the instrument JEM HR-2100 (JEOL Ltd., Tokyo, Japan), operated at 200 kV in bright-field mode. A drop of high-purity distilled water, containing the ultrasonically dispersed particles, was placed onto a holey carbon film supported by a copper-mesh TEM grid (CF300-CU-UL, carbon square mesh, CU, 300 mesh from Electron Microscopy Science, Hatfield, England) and it was air-dried at room temperature.

The N_2 adsorption-desorption isotherms were measured at 77 K on an Autosorb iQ Quantachrome porosimeter (Anton Paar QuantaTec Inc., Boynton Beach, FL, USA). The samples were outgassed at 150 °C for 20 h under vacuum (10^{-6} mbar) before the measurements. Brunauer-Emmett-Teller (S_{BET}) [41] and CPSM method (S_{CPSM}) [42,43] were used for the specific surface area determination ($S_g(m^2/g)$) [44]. Pore size distribution was estimated using both the CPSM model [42,43,45] and the DFT model for cylindrical pores [46]. Total pore volume was estimated from the total adsorbed amount at $P/P_0 \leq 0.998$. Moreover, the micropore volume fraction was evaluated according both to Dubinnin-Raduskevitch [47] and CPSM method [48].

UV-Visible (UV-vis) spectra were measured with halogen lamp in the range 400–700 nm (0.5 nm step), using a two-beam spectrophotometer UV-2401(PC)-Shimadzu (Shimadzu, Kyoto, Japan).

2.4. Batch Experiments

The magnetic hybrid materials mAC-snack and mAC-snack (p.t.) as well as the raw activated carbon AC-snack were tested for their adsorption capacity in hexavalent chromium removal by kinetic experiments in acidic conditions (pH = 3). For these experiments, 18 mg of the adsorbent was dispersed in 100 mL of an around 3 ppm Cr(VI) aqueous solution and reacted for 48 h. During the reaction, and at specific time periods i.e., 0.5, 1.5, 2.5, 3.5, 6, 9, 24 and 48 h, 300 μL of the supernatant solution were photometrically measured by applying the 1,5-diphenylcarbazide method [49]. Subsequently, the mAC-snack material, which exhibited the highest adsorption capacity, was studied using 100 mL Cr(VI) aqueous solutions with 18 mg adsorbent dispersed in it, at different pH values i.e., 1.5, 3.0, 3.6, 4.0 and 5.0, and different Cr(VI) initial concentrations i.e., 2.41, 5.24, 10.88, 19.81, 39.65, 49.31, and 68.72 ppm. The different Cr(VI) initial concentrations of the studied aqueous solutions were obtained by appropriate dilution of a stock Cr(VI) solution (1 mg/mL) with distilled water and the pH value was adjusted by adding 1 N HCl. The batch experiments were performed at 21 °C. After the adsorption process, the suspension was centrifuged and the solid phase were analyzed using FT-IR and Mossbauer spectroscopies as well as VSM magnetic measurements.

2.5. Oxidation Experiments for the Determination of Cr^{3+} in the Solution

After the end of the batch Cr(VI) adsorption experiments, the supernatant solutions were oxidized with $KMnO_4$, in order to determine the diluted Cr^{3+} species. A 3500 ppm $KMnO_4$ aqueous solution, was used as stock solution. Aqueous MnO_4^- solution which exhibited a small equivalent excess i.e., 1.2 × initial Cr(VI) concentration, was reacted for 30 min with each supernatant solution in order to ensure the oxidation of the diluted Cr^{3+} species to Cr^{6+}. The Cr^{6+} concentration was determined using the diphenylcarbazide method.

2.6. Thermodynamics of Cr(VI) Adsorption

Equations (1) and (2) were used for the calculation of Gibbs free energy (ΔG^0) for the adsorption process of Cr(VI) in the mAC-snack material at temperature T = 21 °C and pH = 3,

$$K_D = q_e / C_e \quad (1)$$

and

$$\Delta G^0 = -RT \cdot \ln K_D \quad (2)$$

where C_e (mg/mL) is the concentration of Cr(VI) in the liquid phase at the equilibrium stage, q_e (mg/g) is the amount of Cr(VI) adsorbed in the activated carbon at the equilibrium stage, K_D (mL/g) is the distribution coefficient, R (8.134 J/mol K) is the gas constant, and T is the process temperature in Kelvin (K).

3. Results and Discussion

3.1. Material's Characterization

Porosimetric tests were carried out on mAC-snack, mAC-snack (p.t.), and AC-snack materials. Figure 1 presents the porosimetric study of the most advantageous among these three materials i.e., the mAC-snack material. Similar measurements and estimations were also carried out for the other two materials and the results are presented in Tables 1 and 2. It is obvious from the tabulated values that the AC-snack product exhibits the greater pore volume and the bigger specific surface area. Also we could say that in all cases hierarchical pore structure with micro-meso-macro- pore intraparticle regions was achieved. This result is also obvious from the DFT distribution. According to the pore number distributions in all cases the micropore fraction exhibits a mean pore diameter in the range of D^{CPSM}_{Nmean} = 1.35–1.60 nm. The fraction of the micropore volume predicted using the CPSM model V^{CPSM}_{micro} increases as we go from the mAC-snack to the AC-snack material. This result is consistent with the micropore volume $V^{D\text{-}R}_{micro}$ predictions of the Dubbinin Raduskevitch method.

Table 1. Textural parameters derived from N_2 adsorption-desorption measurements.

Material	S_{gBET} (m^2/g)	S_{CPSM} (m^2/g)	V_{pore} (cm^3/g)	V^{CPSM}_{micro} (% cm^3/g)	$V^{D\text{-}R}_{micro}$ (% cm^3/g)
mAC-snack	426	571	0.357	56	55
mAC-snack (p.t.)	544	754	0.303	76	86
AC-snack	766	1059	0.394	92	93

Table 2. Textural parameters derived from CPSM simulation of N_2 adsorption-desorption overall hysteresis loop and from the DFT method application.

Material	D^{CPSM}_{Nmean} * (nm)	D^{CPSM}_{Vmean} ** (nm)	D^{CPSM}_{Vmicro} (nm)	D^{CPSM}_{Vmeso1} (nm)	D^{CPSM}_{Vmeso2} (nm)	D^{DFT}_{Vmicro} (nm)	D^{DFT}_{Vmeso} (nm)
mAC-snack	1.52	25	1.44	10.7	66.8	0.71/1.2	5.3
mAC-snack (p.t.)	1.39	38	1.30	2.1	16.5	0.70/1.1	5.1
AC-snack	1.41	2	1.38	2.0	8.2	0.69/1.02	2.1

* D^{CPSM}_{Nmean}: mean pore diameter resulted from the pore number distribution (pore population). ** D^{CPSM}_{Vmean}: mean pore diameter resulted from the pore volume distribution.

Results for specific surface area, percentage of micropore volume fraction, and mean pore diameter from number and volume distributions are presented in Tables 1 and 2.

The validation of the three materials as absorbers for the Cr(VI) removal processes was carried out by adsorption kinetic experiments. Approximately equal low concentration aqueous Cr(VI) solutions was prepared as follows, 2.41 ppm to test the mAC-snack material, 2.82 ppm to test the mAC-snack (p.t.) material, and 3.14 ppm to test the AC-snack material. Tests were completed at pH = 3 and temperature T = 21 °C. Figure 2 presents the

fitting results of the Pseudo First Order (PFO) and the Pseudo Second Order (PSO) kinetic models [29] upon the experimental data.

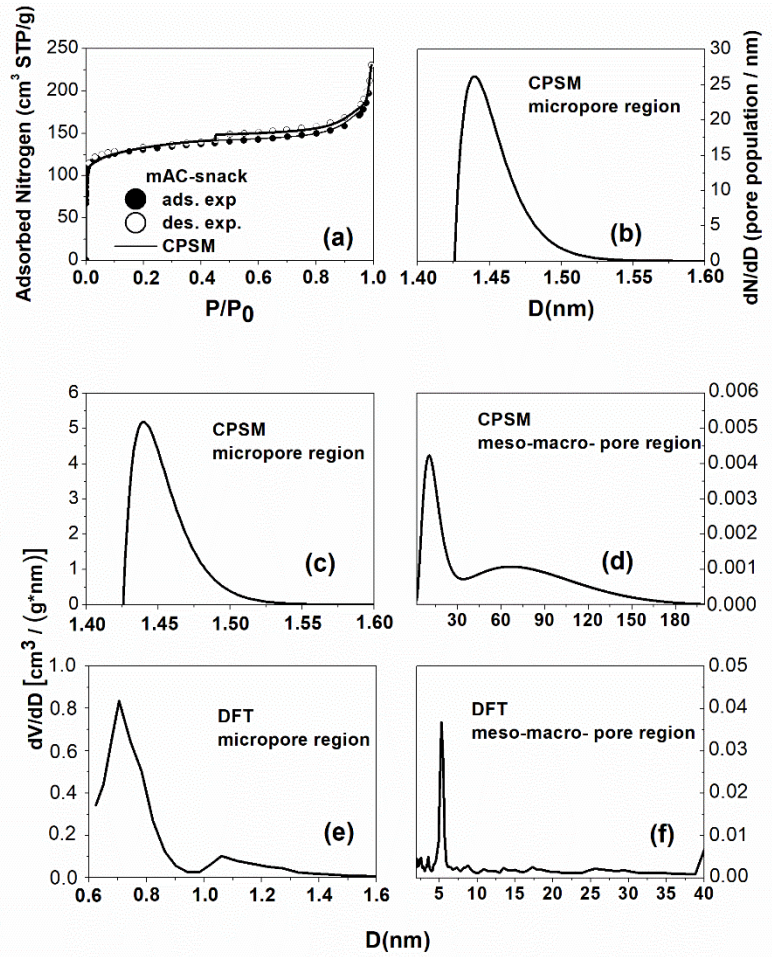

Figure 1. Nitrogen porosimetry results for the mAC-snack, (**a**) hysteresis loop CPSM simulation, (**b**) CPSM pore number (population) distribution, micropore region, (**c**) CPSM pore volume distribution, micropore region, (**d**) CPSM pore volume distribution, meso- macro- pore region, (**e**) DFT pore volume distribution, micropore region, (**f**) DFT pore volume distribution, meso- macro- ropore region.

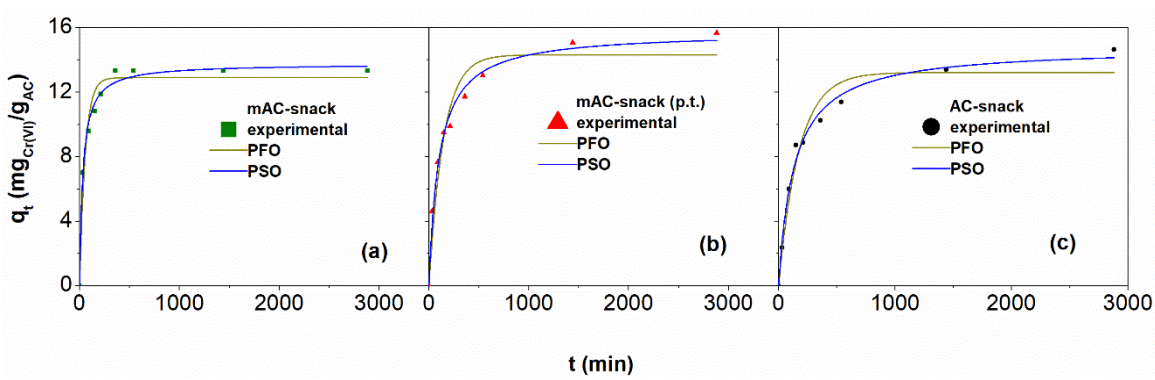

Figure 2. Pseudo First Order (PFO) and Pseudo Second Order (PFO) kinetic models fitted upon the (**a**) mAC-snack, (**b**) mAC-snack (p.t.), and (**c**) AC-snack adsorption experimental data.

Results from these fittings are presented in Table 3 and the PSO adsorption kinetic model is obviously the best fitted model.

Table 3. Pseudo First and Pseudo Second Order kinetics comparison. Adsorption rate constant, Cr(VI) uptake at equilibrium stage, and initial adsorption rate calculation.

Material	PFO R^2	PSO R^2	k_2 $g_{AC} \cdot mg_{Cr(Vi)}{}^{-1} \cdot min^{-1}$	q_e $mg_{Cr(VI)} \cdot g_{AC}{}^{-1}$	r_i $mg_{Cr(VI)} \cdot g_{AC}{}^{-1} \cdot min^{-1}$
mAC-snack	0.9568	0.9900	0.00221	13.77	0.4190
mAC-snack (p.t.)	0.9366	0.98673	6.2966×10^{-4}	15.75	0.1562
AC-snack	0.9570	0.9895	5.0076×10^{-4}	14.80	0.1097

Initial adsorption rate for the three materials were calculated according to the equation reported in literature [29]. Even though the mAC-snack material exhibits the lower specific surface area, it is obvious from Table 3 that this material exhibits the higher initial adsorption activity. This happens because this material includes zero valent iron in its pore structure, as it is shown from XRD pattern below and Mossbauer spectroscopy, which enhance the Cr(VI) adsorption significantly. Continuing this study and because of this reason from this point we dealt with the mAC-snack material only.

The XRD patterns of the activated carbon AC-snack and the magnetic hybrid mAC-snack, are presented in Figure 3. After the chemical carbonization and activation of the AC-snack, XRD pattern didn't exhibited crystalline peaks indicating the amorphous structure of the carbon material. On the other hand, the diffraction pattern of mAC-snack sample, is mainly shown a sharp and intense diffraction peak at 2θ = 44.5° and a weaker peak at 65.5° which, according to the JCPD library file no. 04-007-9753, are derived from reflections (110) and (200) respectively of the crystalline phase of magnetic a-Fe. The crystallite size is calculated equal to ~30 nm by applying Scherrer's equation at the more intense peak i.e., 44.5°. Finally, the XRD pattern of the magnetic hybrid material also exhibits several weaker peaks which are assigned to the crystalline phase of iron carbide (Fe_3C), according to the JCPD library file no. 00-035-0772. These peaks indicating the presence of zero valent iron nanoparticles with this phase. The average crystallite size of this phase is estimated equal to ~29 nm by applying Scherrer's equation at the more intense peaks (42.7° and 43.7°).

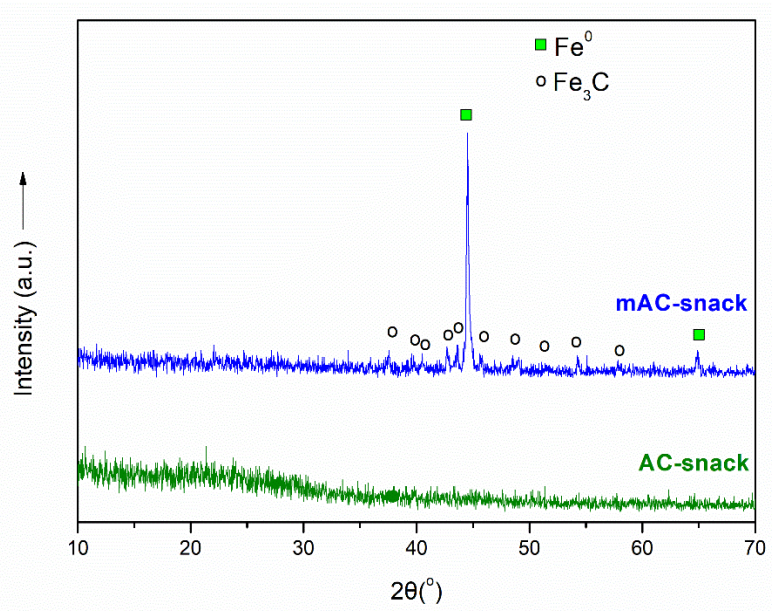

Figure 3. X-ray diffraction patterns the AC-snack and mAC-snack samples.

The FT-IR spectra of the produced magnetic mAC-snack and non-magnetic AC-snack materials as well as the corresponding spectrum of the raw snack material are presented in Figure 4. The spectrum of snack exhibits characteristic absorption bands corresponding

to vibration modes of C-H, C-O-C, C-O bonds on the organic groups. In our case such groups exist in corn and potato starch as well as the several ingredients of snack [50]. In detail, absorption bands at 2853 and 2927 cm^{-1}, correspond to the C-H asymmetric and symmetric stretching vibrations of the (-CH_2-) groups [51,52] whereas at 1457 cm^{-1} to CH_2 symmetric deformation modes [50]. The absorption bands at 1747 cm^{-1} is ascribed to the C=O stretching modes of protonated carboxylate groups which form cyclic dimers [53], while at 1150 and 1045 cm^{-1} to C-O-C and C-O stretching modes. The band at 718 cm^{-1} can be assigned either to aromatic C-H out-of-plane bending vibrations [54] or C-O-C ring vibration of carbohydrates on starch [50]. On the other hand, the infrared spectra of the activated carbon materials, magnetic or not, are similar, showing characteristic absorption bands of carbon-based materials while the vibration modes of the snack raw material are absent. More specifically, the broad band at 1545 cm^{-1}, is assigned either to the stretching vibrations of -COO^- units, close to aromatic carbon rings, or C=C bonds in aromatic rings [53]. Moreover, the broad band at ~1120 cm^{-1} can be assigned to vibration modes of C-H bonds in aromatic carbon rings and/or to C-O bonds in ether, phenyl, alcoholic and ester groups. In the magnetic hybrid's spectra, there are not observed clear absorption bands in the low frequency region (745–400 cm^{-1}) that could be assigned to Fe-O and Fe-C vibrations of the formed iron based nanoparticles (iron carbide (Fe_3C) and iron oxide shell of zero valent iron (Fe^0)) [39,55,56]. This is expected due to the formation of very thin iron oxide shell of zero valent iron phase and/or very small size nanoparticles. Finally, the broad absorption band at ~3420 cm^{-1} which exists in all activated carbon's spectra, is assigned to vibrations of physically adsorbed water molecules.

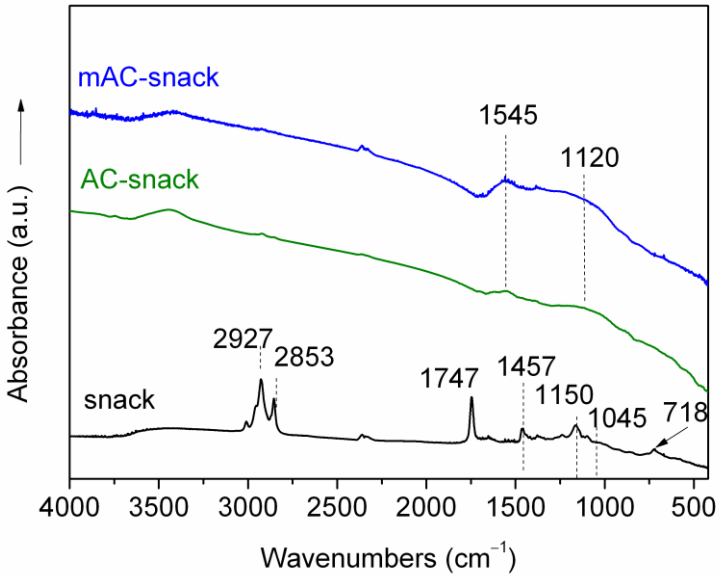

Figure 4. FTIR spectra of AC-snack and mAC-snack samples in comparison with the spectrum of initial snack.

The DTA/TG curves of AC-snack and mAC-snack samples, are shown in Figure 5. The DTA curve of AC-snack (Figure 5a) exhibits one exothermic peak at 472 °C, which corresponds to the carbon combustion of the material, and it is accompanied with 77% mass loss on TG% curve. The ~8% remaining mass could be attributed to potassium carbonates or oxides that were formed during the activation process [57,58]. On the other hand, the carbon matrix combustion is obvious in the DTA curve of the mAC-snack (Figure 5b) by two exothermic peaks at lower temperature (295 and 405 °C) and 48.5% mass loss on TG% curve. This shift of combustion temperature at lower values, could be assigned to the existence of small iron-based magnetic nanoparticles on mAC-snack. The exothermic oxidation of these nanoparticles takes place at lower temperatures and consequently such nanoparticles could act as catalysts for the carbon combustion [39,59]. Finally, the 47.5%

remaining mass in TG% curve of mAC-snack (Figure 5b), is attributed to the presence of thermal stable phase of Fe_3C [60] and iron oxides that either exist in the material or were formed by thermal oxidation during the measurement as well as potassium carbonates or oxides that remained from the carbonization-activation process. Taking into account, the remaining mass on TG% curve of non-magnetic AC-snack material, it is possible to estimate the iron content in mAC-snack materials equal to 30.6 %wt.

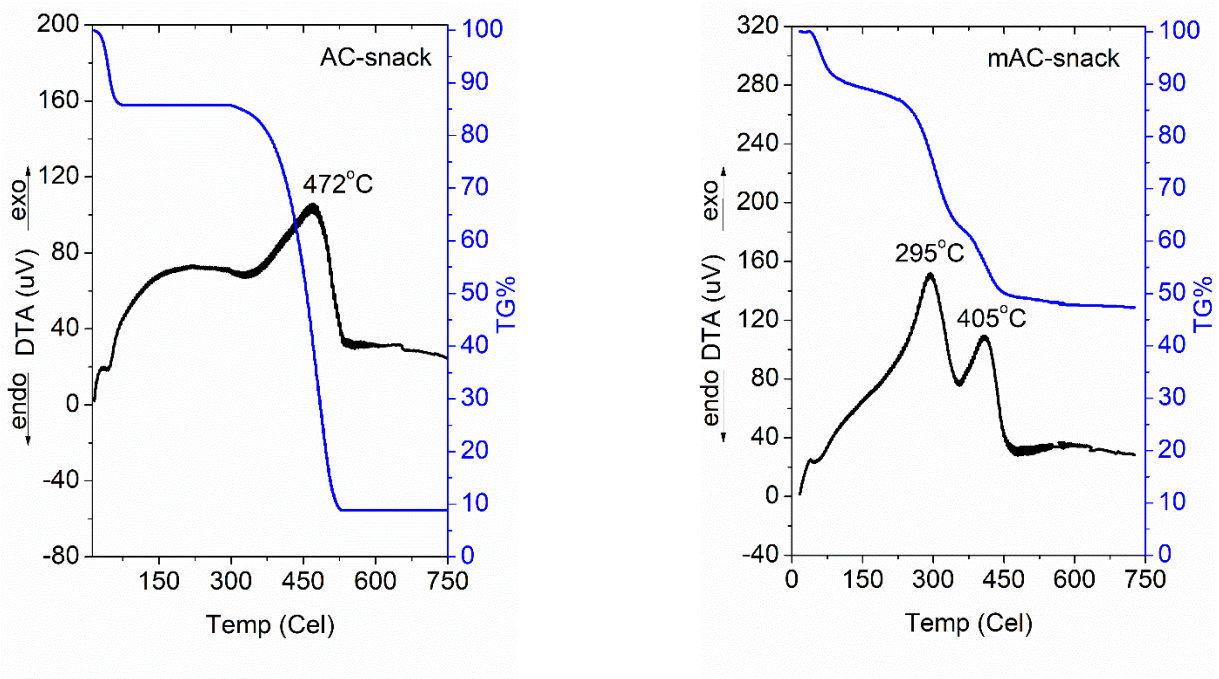

(**a**) (**b**)

Figure 5. DTA and TGA curves of AC-snack (**a**) and mAC-snack (**b**) samples.

The transmission electron microscopy (TEM) images of the magnetic hybrid material mAC-snack are shown in Figure 6. Figure 6a, reveals the formation of spherical nanoparticles having the typical core-shell structure of zero valent iron (Fe^0) phase, exhibiting sizes between ~10–30 nm (~5–20 nm core size and 3–5 nm shell size). These nanoparticles seem to be homogenously dispersed on the carbon matrix (Figure 6a) with only some small clusters formation (clusters from two or three nanoparticles). In Figure 6b, it is observed that nanoparticles with smaller sizes (~3–7.5 nm, dark spots in Figure 6b) than those that have been estimated from XRD results for the two magnetic phases (~30 nm), also formed. These nanoparticles are maybe some small cementite (Fe_3C) or Fe^0 nanoparticles that also formed on the carbon surface. The Fe^0 and Fe_3C phases could be appeared with darker contrast compared to their adjacent phase of carbon or iron oxide due to their large energy densities [61–63]. However, this is a small region of the sample, and it is not referred to the whole material. XRD patterns and ^{57}Fe Mössbauer spectra that are described above and below respectively, represent the total mass of the material and provide the overall information for the average crystallite and particle size of the sample. Finally, it is observed that the carbon matrix exhibits a partial ordered structure, which consists of parallel carbon layers as it shown in Figure 6c.

3.2. Hexavalent Chromium Removal

Experimental measurements for pH effect upon maximum capacity of the hybrid material mAC-snack, indicated that acidic conditions were necessary. As it is shown in Figure 7 pH values lower than 3.6 led to 100% removal of Cr(VI) from aqueous solutions.

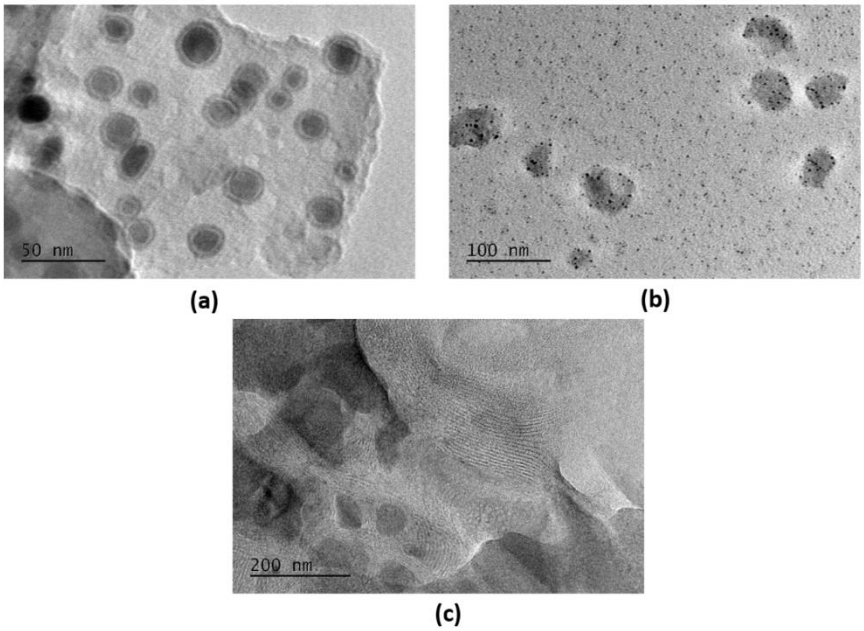

Figure 6. TEM images of the magnetic hybrid mAC-snack with scale bar = 50 nm (**a**), 100 nm (**b**) and 200 nm (**c**).

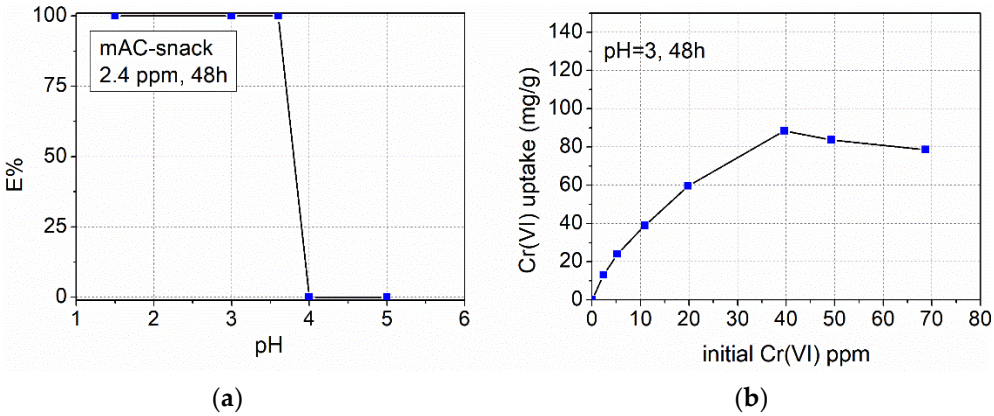

Figure 7. (**a**) Effect of pH value upon maximum removal capacity of Cr(VI) from aqueous solutions. (**b**) Effect of initial Cr(VI) concentration in aqueous solutions upon the maximum uptake capacity of mAC-snack material.

Sequentially, maximum adsorption capacity measurements were carried out at pH = 3 and temperature T = 21 °C for 48 h and for different initial Cr(VI) concentrations (2.41, 5.24, 10.88, 19.81, 39.65, 49.31, 68.72 ppm) according to the procedure reported elsewhere [24]. The results are depicted in Figure 7b and the conclusion was that maximum capacity which was obtained for $C_{init.\ Cr(VI)}$ = 39.65 ppm was q_{max} = 88.382 $mg_{Cr(VI)}/g_{AC}$. Assuming this maximum capacity as fixed value we tested four different adsorption models to estimate the Cr(VI) uptake at the equilibrium stage. The results from this evaluation are depicted in Figure 8a and reported in Table 4. It is obvious from R^2 values that the Langmuir model fitted best the experimental data which means that a monolayer adsorption is the prevailing mechanism.

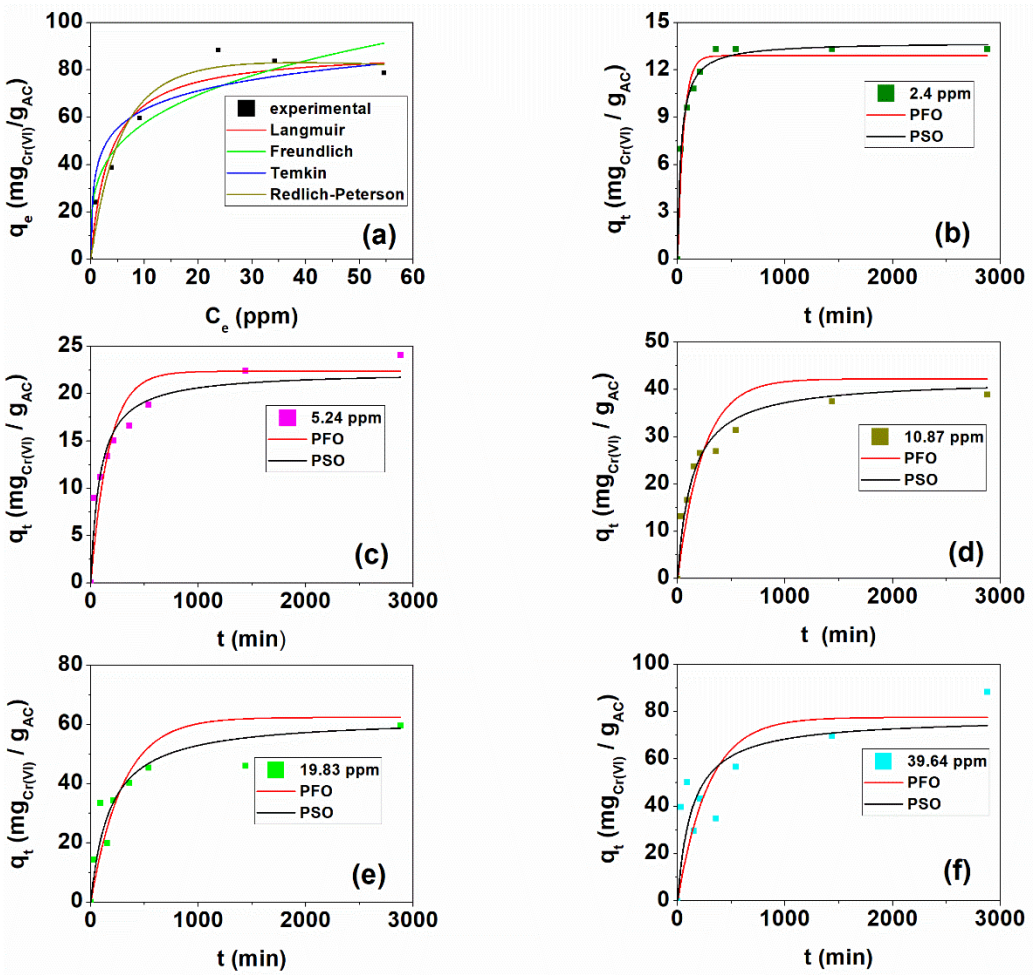

Figure 8. Test for the appropriate adsorption model (**a**) as well as for the appropriate kinetic model (i.e., PFO or PSO) to predict the Cr(VI) removal mechanism from aqueous solutions for different initial Cr(VI) concentrations i.e., 2.41 ppm (**b**), 5.24 ppm (**c**), 10,87 ppm (**d**), 19.83 ppm (**e**), and 39.64 ppm (**f**).

Table 4. Correlation coefficient values resulted from the comparison of four adsorption models assuming maximum uptake capacity q_{max}. Predicted Langmuir adsorption constant K_L.

Material	R^2	q_{max} ($mg_{Cr(VI)}/g_{AC}$)	K_L (ppm^{-1})
Langmuir	0.94944	88.382	0.27987
Freundlich	0.92982	-	
Temkin	0.89601	-	
Redlich-Peterson	0.93406	-	

For adsorbent mass $m_{ads.}$ (mg) in 1000 mL Cr(VI) aqueous solution the calculated C_e (ppm) concentration of Cr(VI) in aqueous solution at equilibrium stage is as follows:

$$C_e(\text{ppm}) = C_{init.}(\text{ppm}) - \frac{m_{ads.}}{1000} * q_e \tag{3}$$

where q_e ($mg_{Cr(VI)}/g_{AC}$) is the Cr(VI) uptake at the equilibrium stage and $C_{init.}$ (ppm) the initial Cr(VI) concentration.

The Langmuir adsorption equation could be modified as follows:

$$q_e = \frac{K_L * q_{max} * \left(C_{init.} - \frac{m_{ads.}}{1000} * q_e\right)}{1 + K_L * \left(C_{init.} - \frac{m_{ads.}}{1000} * q_e\right)} \tag{4}$$

It is obvious from Equation (2) that the total uptake at the equilibrium stage depends on the initial concentration of Cr(VI). Solving the non-linear Equation (2) with numerical methods (i.e., solver software Excel) we obtain different values of q_e for different initial concentrations. The results from this numerical solution are presented in Table 5. Keeping fixed the values of the q_e estimated by Langmuir model we test pseudo first (PFO) and pseudo second (PSO) order kinetic model for five different initial Cr(VI) concentrations. Results are presented in Figure 8b–f. According to the R^2 criterion which is also presented in Table 5 the pseudo second kinetic model predicts more accurate the q_t amount of the adsorbed Cr(VI) versus the time of the adsorption.

Table 5. Total Cr(VI) amount uptake to the mAC-snack adsorbent at equilibrium stage for different initial concentrations.

C_{init}. (ppm)	q_e (Langm.) ($mg_{Cr(VI)}/g_{AC}$)	PFO R^2	PSO R^2	k_2 ($g \cdot mg^{-1} \cdot min^{-1}$)	r_{i2} ($mg \cdot g^{-1} \cdot min^{-1}$)
2.41	10.62	0.95675	0.98995	0.00221	0.2493
5.24	22.38	0.87858	0.95114	5.25274×10^{-4}	0.2631
10.88	42.23	0.82838	0.9527	1.75396×10^{-4}	0.3128
19.81	62.43	0.73202	0.8664	8.94774×10^{-5}	0.3487
39.65	77.58	0.4922	0.63204	9.57968×10^{-5}	0.5766
49.31	80.17	-	-		
68.72	82.88	-	-		

As it is shown in the initial adsorption rate column this rate increases as the initial concentration increases. Moreover, the pseudo second order mechanism indicates that not only physical adsorption occupation of pore surface free sites occurs, but chemical bonding and maybe chemical reactions took place.

A comparison for the adsorption capacity of the magnetic material mAC-snack, with other adsorbents reported in literature, is presented in Table 6. As it shown mAC-snack exhibits higher or similar adsorption efficiency than other activated carbons, magnetic activated carbon hybrids, or bare iron-based nanoparticles.

Table 6. Comparison of the Cr(VI) adsorption capacities (q_m) on mAC-snack with other adsorbents reported in the literature.

Adsorbent	pH	q_m (mg/g)	Ref.
Sodium polyacrylate AC/Fe-Fe_3C	3	90	[38]
Fe/Fe_3C nanoparticles	3	100	[64]
nZVI–Fe_3O_4	3	100	[65]
AC-fiber/nZVI	3	91.5	[66]
Filtrasorb 400-AC/nZVI	4	25	[67]
AC/nZVI	5	24	[68]
AC/Fe-Fe_3O_4	2–6	165–73	[69]
modified AC/nZVI	4	66	[70]
Corn cob-AC/Fe_3O_4	2	57	[71]

Table 6. *Cont.*

Adsorbent	pH	q_m (mg/g)	Ref.
MWCNTs/Fe_3O_4	2	14.28	[72]
AC/Fe_3O_4	2	2.84	[72]
Magnetic nanocomposite prepared with cotton	4	3.74	[73]
Magnetic biochar prepared from Melia azedarach wood	3	25.27	[74]
Cellulose-biochar/ZVI	3	30.83	[75]
Hemicellulose-biochar/ZVI	3	23.77	[75]
Lignin-biochar/ZVI	3	17.68	[75]
Powdered AC	4	46.9	[76]
coconut tree sawdust-AC	3	3.46	[21]
longan seed-AC	3	35.02	[77]
Casuarina equisetifolia leaves-AC	3	17.2	[25]
Poseidonia Oceanica-AC	3	120	[24]
spent coffee-AC	3	109	[29]
mAC-snack	3	88.38	This work

3.3. Thermodynamics of Cr(VI) Adsorption. Results for Gibbs Free Energy

For initial concentrations of Cr(VI) 2.41, 5.24, 10.88, 19.81, 39.65, 49.31, and 68.72 ppm the adsorption process into the mAC-snack exhibits Gibbs free energy ΔG^0 −23.85, −23.51, −22.64, −21.28, −19.17, −18.52, and −17.56 kJ/mol respectively. The negative values confirm the spontaneous nature of the adsorption process. The values lower than −20 kJ/mol indicate the transition to the chemisorption phenomena where the rate control mechanism includes ion-exchange, surface complexation, chemical bonding, and may be reaction phenomena. Values higher than −20 kJ/mol indicate transition to physisorption phenomena where the occupation of the free sites of pore surface is the control mechanism. Thus, according to literature [24,78] ΔG^0 values which were resulted by this study indicate that both physisorption and chemisorption phenomena occur and this is consistent with the Pseudo Second Order (PSO) model which is the preferable model of the sorption kinetic studies. Moreover, it is obvious that as the initial Cr(VI) concentration increases the ΔG^0 values also increase which means that high presence of Cr(VI) ions interfere the chemisorption processes.

3.4. Study of the Removal Mechanism

After the batch experiments with different initial Cr(VI) concentrations i.e., 2.41, 5.24, 10.88, 19.81, and 39.65 ppm, using mAC-snack material, the supernatant solutions were oxidized by MnO_4^- in order to determine the remaining quantity of Cr^{3+} in the solution. As it shown from the results of the redox experiments in Figure 9, the residual Cr^{3+} is increasing following the increase of the initial Cr(VI) concentration. The presence of such quantities of Cr^{3+} in the solutions, indicates that a redox reaction between Cr^{6+} and zero valent iron occurs.

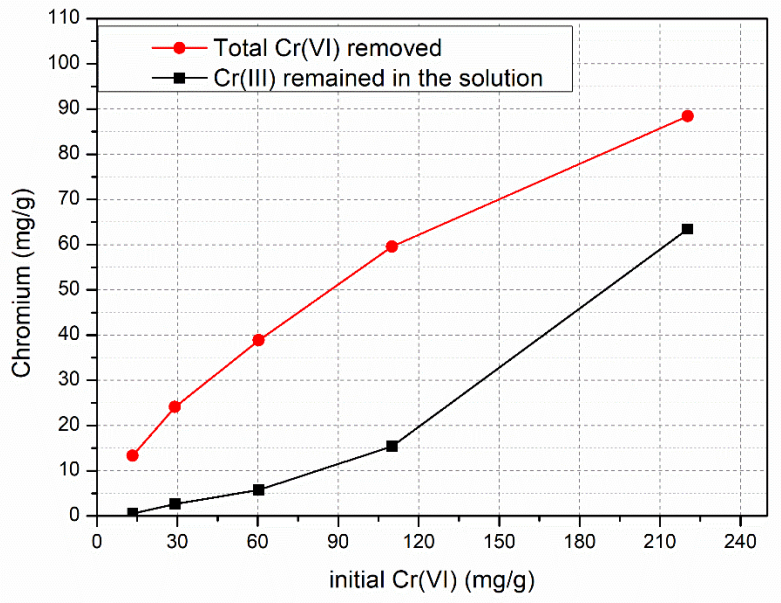

Figure 9. Remaining quantity of Cr(III) in the solution after the sorption experiments with mAC-snack at different initial Cr(VI) concentration in comparison with the total quantity of Cr(VI) removed from the solution.

The comparative FT-IR spectra of the solid adsorbent material mAC-snack, before and after 48 h reaction with Cr(VI) solutions, with different initial Cr(VI) concentrations at pH 3, are presented in Figure 10. In the infrared spectra of the material after Cr(VI) sorption, there are new absorption bands related with the interactions that occur between chromium species and zero valent iron nanoparticles as well as with the surface groups of carbon matrix. More specific, the appearance of the bands at 1700 and 1620 cm^{-1} and the increment of the relative intensities at 1230 and 1030 cm^{-1}, which are ascribed to vibration modes of C=O and C-O bonds on surface groups i.e., carboxyl, carbonyl, ether, hydroxyl [79–81], are related with the interactions of chromium with these groups during the sorption. Due to the acidic conditions of the sorption experiments i.e., pH = 3, the carbon surface is positively charged via its oxygen containing groups, and thus can adsorb the negatively charged chromium oxide species resulting to changes in the infrared spectra on these bands. In general, the protonated and uncoordinated COOH stretching vibration modes are appeared in the range of 1700–1750 cm^{-1}, while the deprotonated and coordinated carboxyl group, COO–M, occurs in the range of 1590–1650 cm^{-1} [82–84]. In our case, the appearance of the band at 1635 cm^{-1} after the chromium sorption, which also becomes more intense as the initial Cr(VI) concentration increased, indicates the possible coordination of chromium species on the carbon's carboxylic groups. On the other hand, considering the interactions with iron nanoparticles, new weak absorption bands appeared at 630 and 540 cm^{-1} in all spectra after Cr(VI) reaction. These bands are assigned to Fe-O vibration modes of magnetic iron oxides, indicating the oxidation of zero-valent iron nanoparticles during the sorption reactions. According to literature, Cr(VI) species are initially adsorbed by zero valent iron nanoparticles, and subsequently are reduced to Cr(III) simultaneously with the oxidation of Fe^0. This fact leads to the precipitation of Cr(III) hydroxides and/or mixed Fe(III)/Cr(III)-(oxy)hydroxides [85].

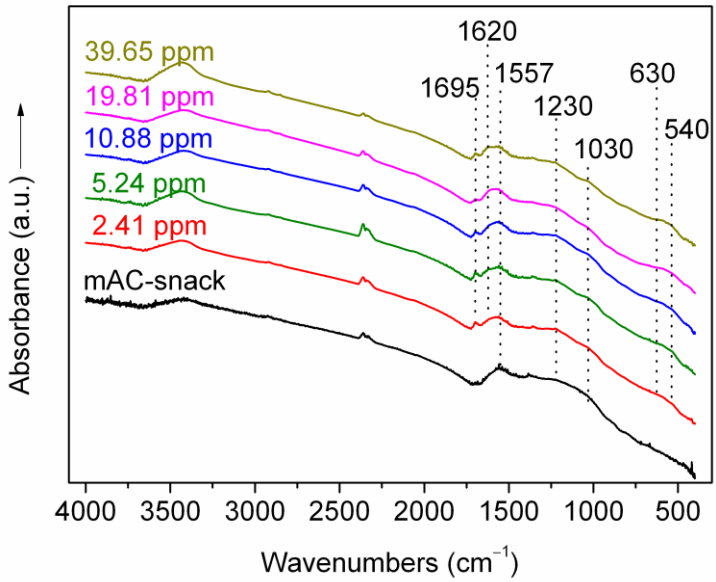

Figure 10. Infrared spectra of the mAC-snack before and after reaction with Cr(VI) solution at pH 3 in different initial concentration.

The ^{57}Fe Mössbauer spectra of the mAC-snack sample are presented in Figure 11a and show a combination of two clearly magnetically split (sextets) and one quadrupole split (doublet) components. The resulting Mössbauer parameter values for these components are listed in Table 7. From these values it is clear that the two sextets correspond to a metallic α-Fe phase and a carbide Fe_3C phase with similar absorption areas (α-Fe: ≈50%, Fe_3C: ≈45%), while the minor doublet corresponds to a Fe^{3+} iron oxide/hydroxide phase with superparamagnetic (SPM) characteristics [86]. The corresponding spectra of the mAC-snack-Cr(VI) sample, after 48 h reaction in Cr(VI) solution with initial Cr(VI) concentration of 5.24 ppm, are presented in Figure 11b. The analyses of these spectra reveal the presence of the same set of components used to fit the spectra of the mAC-snack sample, with the addition of a broad magnetically split component. Resulted Mössbauer parameter values are similar to those of the SPM Fe^{3+} iron oxide/hydroxide phase and collapsing hyperfine magnetic field (B_{hf}) characteristics (COL). In the later sample, the SPM and COL iron oxide/hydroxide components acquire a significant part of the total absorption area i.e., ≈45%, indicating the oxidation of the metallic/alloy α-Fe/Fe_3C phases after the reaction with chromium species. Regarding the absorption areas of the metallic/alloy phases in this sample, the reduced absorption area for the α-Fe phase relative to the Fe_3C phase (α-Fe: ≈25%, Fe_3C: ≈30%), suggests an increased susceptibility in oxidation of the metallic α-Fe phase relative to the carbide Fe_3C phase. This could be a consequence of the reaction with chromium species.

Figure 12 presents the M vs. H loop measurements of the mAC-snack and the mAC-snack-Cr(VI), which correspond to material before and after 48 h of reaction with 5.24 ppm initial Cr(VI) concentration solution respectively. These results were collected at RT. The clear ferromagnetic characteristics of the loops in both samples signify the contributions of the ferromagnetic α-Fe and Fe_3C phases contained in them. The saturation magnetizations (M_S) of $M_S \approx 36$ Am^2/kg for the mAC-snack and $M_S \approx 12$ Am^2/kg for the mAC-snack-Cr(VI) samples are attributed to: (i) the hybrid nature of the samples and (ii) the reduced quantities of the ferromagnetic α-Fe and Fe_3C phases, and (iii) the corresponding increased quantities of the iron oxide/hydroxide phases which were presented in the mAC-snack-Cr(VI) sample. These phases were relative to those in the mAC-snack due to the oxidation of the formers as a consequence of the reaction with Cr(VI) species. The non-vanishing coercivity (H_C) reflects the contribution of the nanostructured nature of the magnetic phases in both samples. Moreover, the increased coercivity for the mAC-snack-Cr(VI) sample i.e., $H_C \approx 30$ mT, compared to that of the mAC-snack sample i.e., $H_C \approx 20$ mT, could

indicate the presence of a distribution of Fe^0 ferromagnetic multidomain nanoparticles with reduced particle sizes from the mAC-snack-Cr(VI) to the mAC-snack [87]. The iron core in the mAC-snack larger particles is gone through a size reduction procedure as a result of the oxidation reaction with Cr(VI) species.

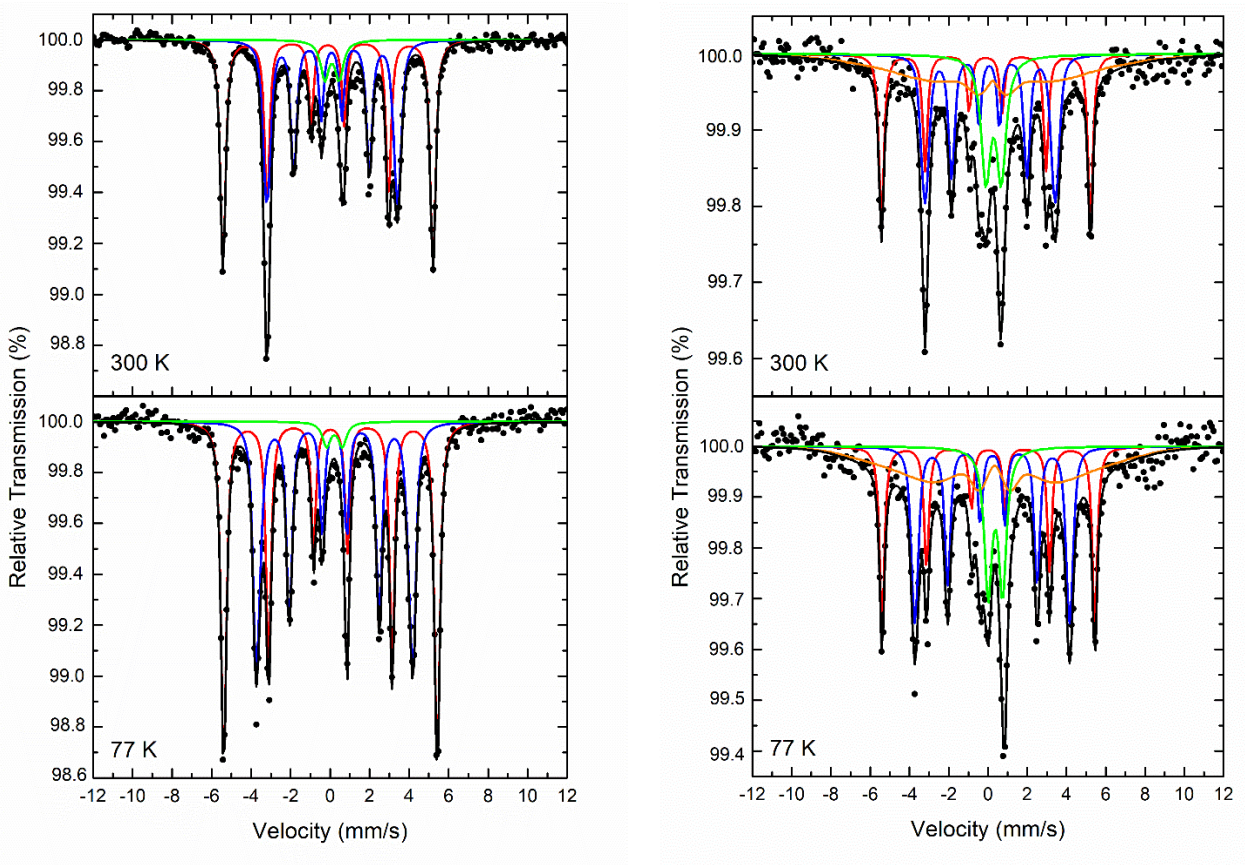

Figure 11. ^{57}Fe Mössbauer spectra of mAC-snack before (**a**) and after (**b**) 48 h reaction with 5.24 ppm Cr(VI) solution, recorded at 300 and 77 K.

Table 7. Mössbauer hyperfine parameters resulting from the best fits of the corresponding spectra of mAC-snack before and after 48 h reaction with 6 ppm Cr(VI) solution recorded at 300 and 77 K. IS is the isomer shift (given relative to α-Fe at 300 K), Γ/2 is the half line-width, 2ε and QS are the quadrupole shift and quadrupole splitting respectively, B_{hf} is the central value of the hyperfine magnetic field, ΔB_{hf} is the spreading of B_{hf}, and Area is the relative spectral absorption area of each component used to fit each spectrum. Typical errors are ± 0.02 mm/s for IS, Γ/2, and 2ε, ± 3 kOe for B_{hf} and ± 5% for Area.

Sample	T (K)	Component (Color)	IS (mm/s)	Γ/2 (mm/s)	2ε or QS (mm/s)	B_{hf} (kOe)	ΔB_{hf} (kOe)	Area (%)
mAC-snack	300	α-Fe (red)	−0.01	0.14	0.01	330	3	49
		Fe_3C (blue)	0.20	0.14	0.04	206	8	45
		SPM Fe^{3+} oxide/hydroxide (green)	0.20	0.25	0.74	0	0	6
	77	α-Fe (red)	0.13	0.14	0.01	336	3	51
		Fe_3C (blue)	0.33	0.14	0.01	254	13	46
		SPM Fe^{3+} oxide/hydroxide (green)	0.33	0.25	0.80	0	0	3

Table 7. *Cont.*

Sample	T (K)	Component (Color)	IS (mm/s)	Γ/2 (mm/s)	2ε or QS (mm/s)	B_{hf} (kOe)	ΔB_{hf} (kOe)	Area (%)
mAC-snack-Cr(VI)	300	α-Fe (red)	−0.01	0.14	0.02	331	2	24
		Fe_3C (blue)	0.19	0.14	0.04	206	9	30
		COL Fe^{3+} oxide/hydroxide (orange)	0.34	0.15	0.00	260	184	29
		SPM Fe^{3+} oxide/hydroxide (green)	0.39	0.29	0.79	0	0	17
	77	α-Fe (red)	0.12	0.14	0.02	337	1	24
		Fe_3C (blue)	0.33	0.14	0.00	245	7	30
		COL Fe^{3+} oxide/hydroxide (orange)	0.42	0.15	−0.03	296	136	31
		SPM Fe^{3+} oxide/hydroxide (green)	0.48	0.23	0.73	0	0	15

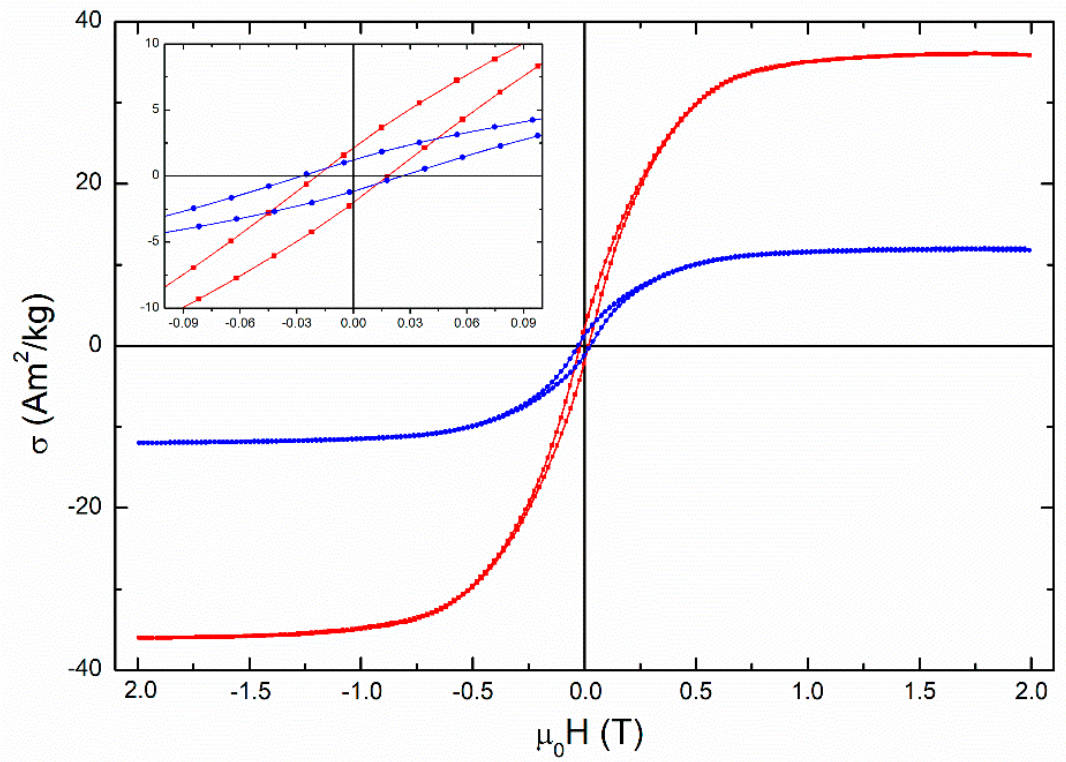

Figure 12. M vs. H loops of mAC-snack (red squares) and mAC-snack-Cr(VI) (blue cycles) samples recorded at room temperature. The inset presents a magnification focused on the loops' center to reveal their coercive characteristics.

4. Conclusions

An expired polysaccharide food product i.e., cheese-tomato flavor corn snack, was studied as a precursor to produce a high specific surface area activated carbon i.e., S_{BET} = 800 m^2/g, and a magnetic carbon hybrid material, for use in an hexavalent chromium removal process due to environmental remediation activities. The chemical activation of the char, which was derived from the snack via pyrolysis process, was carried out using potassium hydroxide under the presence of iron acetate complex species, and leads to the development of a novel porous magnetic hybrid carbon. This new material exhibits micro-meso-macro- pore intraparticle regions, remarkable microporous structure, high specific surface area i.e., S_{BET} = 500 m^2/g, and

high efficiency in hexavalent chromium removal. According to the XRD and Mossbauer results, the hybrid material mainly consists of a metallic α-Fe phase and a carbide Fe_3C phase with similar contents i.e., α-Fe: ≈50% and Fe_3C: ≈45%, and only few Fe^{3+} iron oxide/hydroxide phase with superparamagnetic characteristics. The VSM magnetization measurements shown that the material has clear ferromagnetic characteristics with saturation magnetizations (M_S) of $M_S \approx 36$ Am^2/kg. TEM images reveal the formation of spherical core-shell zero-valent iron nanoparticles, ~10–30 nm in size, and homogenously dispersed on the carbon matrix. The hybrid magnetic material exhibits high efficiency for Cr(VI) removal, with maximum sorption capacity ~89 mg/g at pH 3. Kinetic study from the batch experiments reveals that the Pseudo Second Order model is the preferable model for the sorption while ΔG^0 values indicate that both physisorption and chemisorption phenomena occur. Oxidation experiments of the reacted solutions after the batch experiments shown the formation of Cr^{3+} ions in the solution which indicates the presence of a reduction process of Cr^{6+} to Cr^{3+}, while FT-IR, Mossbauer and VSM measurements on the magnetic hybrid after the reaction reveal the formation of iron oxide/hydroxide components in a significant part of the material. These findings indicate the oxidation of α-Fe/Fe_3C phases (α-Fe: ≈25%, Fe_3C: ≈30%) during the reaction with chromium species and at the same time the reduction of Cr^{6+} to Cr^{3+}. Finally, according to the present study this kind of expired snack could be recycled for the production of novel hybrid magnetic carbon with effective sorption properties for environmental remediation applications.

Author Contributions: Conceptualization, M.A.K. and A.B.B.; Methodology, M.A.K., A.B.B. and A.K.; Formal Analysis, M.A.K., C.E.S. and A.P.D.; Investigation, G.A., A.K., M.B., K.M., D.M. and A.A.; Resources, M.A.K.; Writing—Original Draft Preparation, M.B., C.E.S. and A.P.D.; Writing—Review and Editing, M.A.K., A.B.B., C.E.S. and M.B.; Visualization, M.A.K., C.E.S. and A.P.D.; Supervision, M.A.K. and A.B.B.; Project Administration, M.A.K.; Funding Acquisition, M.A.K. and M.B. All authors have read and agreed to the published version of the manuscript.

Funding: This project has received funding from the Hellenic Foundation for Research and Innovation (HFRI, Greece) and the General Secretariat for Research and Innovation (GSRI, Greece), under grant agreement No [1508]. In addition, this study was funded by the project "National Infrastructure in Nanotechnology, Advanced Materials and Micro-/Nanoelectronics" (MIS-5002772) which was implemented under the action "Reinforcement of the Research and Innovation Infrastructure", funded by the Operational Programme "Competitiveness, Entrepreneurship and Innovation" (NSRF 2014–2020), and co-financed by Greece and the European Union (European Regional Development Fund).

Institutional Review Board Statement: Not applicable.

Data Availability Statement: The data presented in this study are available on request from the corresponding author.

Acknowledgments: The authors greatly acknowledge Ch. Papachristodoulou for the XRD measurements and the use of the XRD and VSM Laboratory Network Units of the University of Ioannina.

Conflicts of Interest: The authors declare no conflict of interest.

References

1. Jjagwe, J.; Olupot, P.; Menya, E.; Kalibbala, H. Synthesis and Application of Granular Activated Carbon from Biomass Waste Materials for Water Treatment: A Review. *J. Bioresour. Bioprod.* **2021**, *6*, 292–322. [CrossRef]
2. Uriburu-Gray, M.; Pinar-Serrano, A.; Cavus, G.; Knipping, E.; Aucher, C.; Conesa-Cabeza, A.; Satti, A.; Amantia, D.; Martínez-Crespiera, S. Mesoporous Carbons from Polysaccharides and Their Use in Li-O2 Batteries. *Nanomaterials* **2020**, *10*, 2036. [CrossRef] [PubMed]
3. Benítez, A.; Amaro-Gahete, J.; Chien, Y.-C.; Caballero, Á.; Morales, J.; Brandell, D. Recent advances in lithium-sulfur batteries using biomass-derived carbons as sulfur host. *Renew. Sustain. Energy Rev.* **2022**, *154*, 111783. [CrossRef]
4. Ouyang, J.; Zhou, L.; Liu, Z.; Heng, J.; Chen, W. Biomass-derived activated carbons for the removal of pharmaceutical mircopollutants from wastewater: A review. *Sep. Purif. Technol.* **2020**, *253*, 117536. [CrossRef]
5. Secondi, L. Expiry Dates, Consumer Behavior, and Food Waste: How Would Italian Consumers React If There Were No Longer "Best Before" Labels? *Sustainability* **2019**, *11*, 6821. [CrossRef]
6. Stenmarck, Â.; Jensen, C.; Quested, T.; Moates, G.; Buksti, M.; Cseh, B.; Scherhaufer, S. *Estimates of European Food Waste Levels*; IVL Swedish Environmental Research Institute: Stockholm, Sweden, 2016.

7. Lovegrove, A.; Edwards, C.H.; De Noni, I.; Patel, H.; El, S.N.; Grassby, T.; Zielke, C.; Ulmius, M.; Nilsson, L.; Butterworth, P.J.; et al. Role of polysaccharides in food, digestion, and health. *Crit. Rev. Food Sci. Nutr.* **2017**, *57*, 237–253. [CrossRef]
8. Brouns, F. Saccharide Characteristics and Their Potential Health Effects in Perspective. *Front. Nutr.* **2020**, *7*, 75. [CrossRef]
9. Lee, J.; Kim, J.; Hyeon, T. Recent progress in the synthesis of porous carbon materials. *Adv. Mater.* **2006**, *18*, 2073–2094. [CrossRef]
10. Gan, Y.X. Activated Carbon from Biomass Sustainable Sources. *J. Carbon Res.* **2021**, *7*, 39. [CrossRef]
11. Saleem, J.; Shahid, U.B.; Hijab, M.; Mackey, H.; McKay, G. Production and applications of activated carbons as adsorbents from olive stones. *Biomass Convers. Biorefin.* **2019**, *9*, 775–802. [CrossRef]
12. Sun, H.; Brocato, J.; Costa, M. Oral Chromium Exposure and Toxicity. *Curr. Environ. Health Rep.* **2015**, *2*, 295–303. [CrossRef] [PubMed]
13. GracePavithra, K.; Jaikumar, V.; Kumar, P.S.; SundarRajan, P. A review on cleaner strategies for chromium industrial wastewater: Present research and future perspective. *J. Clean. Prod.* **2019**, *228*, 580–593. [CrossRef]
14. Dakiky, M.; Khamis, M.; Manassra, A.; Mer'eb, M. Selective adsorption of chromium(VI) in industrial wastewater using low-cost abundantly available adsorbents. *Adv. Environ. Res.* **2002**, *6*, 533–540. [CrossRef]
15. Pariser, H.H.; Backeberg, N.R.; Masson, O.C.M.; Bedder, J.C.M. Changing nickel and chromium stainless steel markets-A review. *J. South. Afr. Inst. Min. Metall.* **2018**, *118*, 563–568. [CrossRef]
16. Ghosh, P.K. Hexavalent chromium [Cr(VI)] removal by acid modified waste activated carbons. *J. Hazard. Mater.* **2009**, *171*, 116–122. [CrossRef]
17. Al-Othman, Z.A.; Ali, R.; Naushad, M. Hexavalent chromium removal from aqueous medium by activated carbon prepared from peanut shell: Adsorption kinetics, equilibrium and thermodynamic studies. *Chem. Eng. J.* **2012**, *184*, 238–247. [CrossRef]
18. Aroua, M.K.; Zuki, F.M.; Sulaiman, N.M. Removal of chromium ions from aqueous solutions by polymer-enhanced ultrafiltration. *J. Hazard. Mater.* **2007**, *147*, 752–758. [CrossRef]
19. Pehlivan, E.; Cetin, S. Sorption of Cr(VI) ions on two Lewatit-anion exchange resins and their quantitative determination using UV-visible spectrophotometer. *J. Hazard. Mater.* **2009**, *163*, 448–453. [CrossRef]
20. Rai, M.K.; Shahi, G.; Meena, V.; Meena, R.; Chakraborty, S.; Singh, R.S.; Rai, B.N. Removal of hexavalent chromium Cr (VI) using activated carbon prepared from mango kernel activated with H3PO4. *Resour.-Effic. Technol.* **2016**, *2*, S63–S70. [CrossRef]
21. Selvi, K.; Pattabhi, S.; Kadirvelu, K. Removal of Cr(VI) from aqueous solution by adsorption onto activated carbon. *Bioresour. Technol.* **2001**, *80*, 87–89. [CrossRef]
22. Babel, S.; Kurniawan, T.A. Cr(VI) removal from synthetic wastewater using coconut shell charcoal and commercial activated carbon modified with oxidizing agents and/or chitosan. *Chemosphere* **2004**, *54*, 951–967. [CrossRef] [PubMed]
23. Anandkumar, J.; Mandal, B. Removal of Cr(VI) from aqueous solution using Bael fruit (Aegle marmelos correa) shell as an adsorbent. *J. Hazard. Mater.* **2009**, *168*, 633–640. [CrossRef] [PubMed]
24. Asimakopoulos, G.; Baikousi, M.; Salmas, C.; Bourlinos, A.B.; Zboril, R.; Karakassides, M.A. Advanced Cr(VI) sorption properties of activated carbon produced via pyrolysis of the "Posidonia oceanica" seagrass. *J. Hazard. Mater.* **2021**, *405*, 124274. [CrossRef]
25. Ranganathan, K. Chromium removal by activated carbons prepared from Casurina equisetifolia leaves. *Bioresour. Technol.* **2000**, *73*, 99–103. [CrossRef]
26. Baral, S.S.; Das, S.N.; Rath, P. Hexavalent chromium removal from aqueous solution by adsorption on treated sawdust. *Biochem. Eng. J.* **2006**, *31*, 216–222. [CrossRef]
27. Dubey, S.P.; Gopal, K. Adsorption of chromium(VI) on low cost adsorbents derived from agricultural waste material: A comparative study. *J. Hazard. Mater.* **2007**, *145*, 465–470. [CrossRef]
28. Esmaeili, A.; Ghasemi, S.; Rustaiyan, A. Removal of Hexavalent Chromium Using Activated Carbons Derived From Marine Algae Gracilaria and Sargassum Sp. *J. Mar. Sci. Technol.* **2010**, *18*, 587–592. [CrossRef]
29. Asimakopoulos, G.; Baikousi, M.; Kostas, V.; Papantoniou, M.; Bourlinos, A.B.; Zbořil, R.; Karakassides, M.A.; Salmas, C.E. Nanoporous Activated Carbon Derived via Pyrolysis Process of Spent Coffee: Structural Characterization. Investigation of Its Use for Hexavalent Chromium Removal. *Appl. Sci.* **2020**, *10*, 8812. [CrossRef]
30. Laurent, S.; Forge, D.; Port, M.; Roch, A.; Robic, C.; Vander Elst, L.; Muller, R.N. Magnetic Iron Oxide Nanoparticles: Synthesis, Stabilization, Vectorization, Physicochemical Characterizations, and Biological Applications. *Chem. Rev.* **2008**, *108*, 2064–2110. [CrossRef]
31. Kudr, J.; Haddad, Y.; Richtera, L.; Heger, Z.; Cernak, M.; Adam, V.; Zitka, O. Magnetic Nanoparticles: From Design and Synthesis to Real World Applications. *Nanomaterials* **2017**, *7*, 243. [CrossRef]
32. Bae, S.; Collins, R.N.; Waite, T.D.; Hanna, K. Advances in Surface Passivation of Nanoscale Zerovalent Iron: A Critical Review. *Environ. Sci. Technol.* **2018**, *52*, 12010–12025. [CrossRef] [PubMed]
33. Ali, A.; Zafar, H.; Zia, M.; Haq, I.; Phull, A.; Sarfraz Ali, J.; Hussain, A. Synthesis, characterization, applications, and challenges of iron oxide nanoparticles. *Nanotechnol. Sci. Appl.* **2016**, *9*, 49–67. [CrossRef] [PubMed]
34. Pan, B.; Chen, D.; Zhang, H.; Wu, J.; He, F.; Wang, J.; Chen, J. Stability of hydrous ferric oxide nanoparticles encapsulated inside porous matrices: Effect of solution and matrix phase. *Chem. Eng. J.* **2018**, *347*, 870–876. [CrossRef]
35. Shi, J.; Wang, J.; Wang, W.; Teng, W.; Zhang, W.-X. Stabilization of nanoscale zero-valent iron in water with mesoporous carbon (nZVI@MC). *J. Environ. Sci.* **2019**, *81*, 28–33. [CrossRef]
36. Zhang, D.; Wei, S.; Kaila, C.; Su, X.; Wu, J.; Karki, A.B.; Young, D.P.; Guo, Z. Carbon-stabilized iron nanoparticles for environmental remediation. *Nanoscale* **2010**, *2*, 917–919. [CrossRef]

37. Atkinson, J.D.; Fortunato, M.E.; Dastgheib, S.A.; Rostam-Abadi, M.; Rood, M.J.; Suslick, K.S. Synthesis and characterization of iron-impregnated porous carbon spheres prepared by ultrasonic spray pyrolysis. *Carbon* **2011**, *49*, 587–598. [CrossRef]
38. Asimakopoulos, G.; Karakassides, A.; Baikousi, M.; Gioti, C.; Moschovas, D.; Avgeropoulos, A.; Bourlinos, A.B.; Douvalis, A.P.; Salmas, C.E.; Karakassides, M.A. Nanoporous Carbon Magnetic Hybrid Derived from Waterlock Polymers and Its Application for Hexavalent Chromium Removal from Aqueous Solution. *J. Carbon Res.* **2021**, *7*, 69. [CrossRef]
39. Baikousi, M.; Bourlinos, A.B.; Douvalis, A.; Bakas, T.; Anagnostopoulos, D.F.; Tuček, J.; Šafaářovaá, K.; Zbořil, R.; Karakassides, M.A. Synthesis and Characterization of γ-Fe_2O_3/Carbon Hybrids and Their Application in Removal of Hexavalent Chromium Ions from Aqueous Solutions. *Langmuir* **2012**, *28*, 3918–3930. [CrossRef]
40. Douvalis, A.; Polymeros, A.; Bakas, T. IMSG09: A 57Fe119Sn Mössbauer spectra computer fitting program with novel interactive user interface. *J. Phys. Conf. Ser.* **2010**, *217*, 012014. [CrossRef]
41. Brunauer, S.; Emmett, P.H.; Teller, E. Adsorption of Gases in Multimolecular Layers. *J. Am. Chem. Soc.* **1938**, *60*, 309–319. [CrossRef]
42. Androutsopoulos, G.P.; Salmas, C.E. A New Model for Capillary Condensation−Evaporation Hysteresis Based on a Random Corrugated Pore Structure Concept: Prediction of Intrinsic Pore Size Distributions. 1. Model Formulation. *Ind. Eng. Chem. Res.* **2000**, *39*, 3747–3763. [CrossRef]
43. Androutsopoulos, G.P.; Salmas, C.E. A New Model for Capillary Condensation−Evaporation Hysteresis Based on a Random Corrugated Pore Structure Concept: Prediction of Intrinsic Pore Size Distribution. 2. Model Application. *Ind. Eng. Chem. Res.* **2000**, *39*, 3764–3777. [CrossRef]
44. DOWNLOADS, CPSM_Nitrogen. Available online: http://users.uoi.gr/ksalmas/ (accessed on 20 June 2020).
45. Salmas, C.E.; Androutsopoulos, G.P. Rigid Sphere Molecular Model Enables an Assessment of the Pore Curvature Effect upon Realistic Evaluations of Surface Areas of Mesoporous and Microporous Materials. *Langmuir* **2005**, *21*, 11146–11160. [CrossRef] [PubMed]
46. Dombrowski, R.J.; Hyduke, D.R.; Lastoskie, C.M. Pore Size Analysis of Activated Carbons from Argon and Nitrogen Porosimetry Using Density Functional Theory. *Langmuir* **2000**, *16*, 5041–5050. [CrossRef]
47. Chen, S.G.; Yang, R.T. Theoretical Basis for the Potential Theory Adsorption Isotherms. The Dubinin-Radushkevich and Dubinin-Astakhov Equations. *Langmuir* **1994**, *10*, 4244–4249. [CrossRef]
48. Salmas, C.E.; Ladavos, A.K.; Skaribas, S.P.; Pomonis, P.J.; Androutsopoulos, G.P. Evaluation of Microporosity, Pore Tortuosity, and Connectivity of Montmorillonite Solids Pillared with LaNiOx Binary Oxide. A Combined Application of the CPSM Model, the αs-Plot Method and a Pore Percolation−Connectivity Model. *Langmuir* **2003**, *19*, 8777–8786. [CrossRef]
49. Clesceri, L.S.; Greenberg, A.E.; Eaton, A.D. *Standard Methods for the Examination of Water and Wastewater*, 20th ed.; American Public Health Association: Washington, DC, USA, 1998.
50. Abdullah, A.H.; Chalimah, S.; Primadona, I.; Hanantyo, M. Physical and chemical properties of corn, cassava, and potato starchs. *IOP Conf. Ser. Earth Environ. Sci.* **2018**, *160*, 012003. [CrossRef]
51. Feairheller, W.R.; Katon, J.E. The vibrational spectra of acrylic acid and sodium acrylate. *Spectrochim. Acta Part A Mol. Spectrosc.* **1967**, *23*, 2225–2232. [CrossRef]
52. Grabowska, B.; Holtzer, M. Structural examination of the cross-linking reaction mechanism of polyacrylate binding agents. *Arch. Metall. Mater.* **2009**, *54*, 427–437.
53. Dandekar, A.; Baker, R.T.K.; Vannice, M.A. Characterization of activated carbon, graphitized carbon fibers and synthetic diamond powder using TPD and DRIFTS. *Carbon* **1998**, *36*, 1821–1831. [CrossRef]
54. Budarin, V.; Clark, J.H.; Hardy, J.J.E.; Luque, R.; Milkowski, K.; Tavener, S.J.; Wilson, A.J. Starbons: New starch-derived mesoporous carbonaceous materials with tunable properties. *Angew. Chem. Int. Ed.* **2006**, *45*, 3782–3786. [CrossRef] [PubMed]
55. Li, Y.-S.; Church, J.S.; Woodhead, A.L. Infrared and Raman spectroscopic studies on iron oxide magnetic nano-particles and their surface modifications. *J. Magn. Magn. Mater.* **2012**, *324*, 1543–1550. [CrossRef]
56. Zhang, X.; Yan, Q.; Li, J.; Zhang, J.; Cai, Z. Catalysts on Formation of Carbon-Encapsulated Iron Nanoparticles from Kraft Lignin. *Materials* **2018**, *11*, 139. [CrossRef] [PubMed]
57. Gao, Y.; Yue, Q.; Gao, B.; Li, A. Insight into activated carbon from different kinds of chemical activating agents: A review. *Sci. Total Environ.* **2020**, *746*, 141094. [CrossRef]
58. Chen, W.; Gong, M.; Li, K.; Xia, M.; Chen, Z.; Xiao, H.; Fang, Y.; Chen, Y.; Yang, H.; Chen, H. Insight into KOH activation mechanism during biomass pyrolysis: Chemical reactions between O-containing groups and KOH. *Appl. Energy* **2020**, *278*, 115730. [CrossRef]
59. Ennas, G.; Marongiu, G.; Musinu, A. Characterization of nanocrystalline γ–Fe_2O_3 prepared by wet chemical method. *J. Mater. Res.* **1998**, *14*, 1570. [CrossRef]
60. Tongsri, R.; Vetayanugul, B. Thermal analysis of Fe-carbide and Fe-C mixtures. *J. Met. Mater. Miner.* **2010**, *20*, 45–49.
61. Franken, L.E.; Grünewald, K.; Boekema, E.J.; Stuart, M.C.A. A Technical Introduction to Transmission Electron Microscopy for Soft-Matter: Imaging, Possibilities, Choices, and Technical Developments. *Small* **2020**, *16*, 1906198. [CrossRef]
62. Defilippi, C.; Mukadam, M.O.; Nicolae, S.A.; Lees, M.R.; Giordano, C. Iron Carbide@Carbon Nanocomposites: A Tool Box of Functional Materials. *Materials* **2019**, *12*, 323. [CrossRef]
63. Misof, B.M.; Roschger, P.; Fratzl, P. Imaging Mineralized Tissues in Vertebrates. *Compr. Biomater.* **2011**, *3*, 407–426. [CrossRef]

64. Liu, D.-H.; Guo, Y.; Zhang, L.-H.; Li, W.-C.; Sun, T.; Lu, A.-H. Switchable Transport Strategy to Deposit Active Fe/Fe3C Cores into Hollow Microporous Carbons for Efficient Chromium Removal. *Small* **2013**, *9*, 3852–3857. [CrossRef] [PubMed]
65. Lv, X.; Xu, J.; Jiang, G.; Tang, J.; Xu, X. Highly active nanoscale zero-valent iron (nZVI)–Fe3O4 nanocomposites for the removal of chromium(VI) from aqueous solutions. *J. Colloid Interface Sci.* **2012**, *369*, 460–469. [CrossRef] [PubMed]
66. Huang, L.; Zhou, S.; Jin, F.; Huang, J.; Bao, N. Characterization and mechanism analysis of activated carbon fiber felt-stabilized nanoscale zero-valent iron for the removal of Cr(VI) from aqueous solution. *Colloids Surf. A Physicochem. Eng. Asp.* **2014**, *447*, 59–66. [CrossRef]
67. Mortazavian, S.; An, H.; Chun, D.; Moon, J. Activated carbon impregnated by zero-valent iron nanoparticles (AC/nZVI) optimized for simultaneous adsorption and reduction of aqueous hexavalent chromium: Material characterizations and kinetic studies. *Chem. Eng. J.* **2018**, *353*, 781–795. [CrossRef]
68. Xu, C.-H.; Zhu, L.-J.; Wang, X.-H.; Lin, S.; Chen, Y.-M. Fast and Highly Efficient Removal of Chromate from Aqueous Solution Using Nanoscale Zero-Valent Iron/Activated Carbon (NZVI/AC). *Water. Air. Soil Pollut.* **2014**, *225*, 1845. [CrossRef]
69. Cui, Y.; He, H.; Atkinson, J.D. Iron/Carbon Composites for Cr(VI) Removal Prepared from Harmful Algal Bloom Biomass via Metal Bioaccumulation or Biosorption. *ACS Sustain. Chem. Eng.* **2019**, *7*, 1279–1288. [CrossRef]
70. Jiao, C.; Tan, X.; Lin, A.; Yang, W. Preparation of Activated Carbon Supported Bead String Structure Nano Zero Valent Iron in a Polyethylene Glycol-Aqueous Solution and Its Efficient Treatment of Cr(VI) Wastewater. *Molecules* **2020**, *25*, 47. [CrossRef]
71. Nethaji, S.; Sivasamy, A.; Mandal, A.B. Preparation and characterization of corn cob activated carbon coated with nano-sized magnetite particles for the removal of Cr(VI). *Bioresour. Technol.* **2013**, *134*, 94–100. [CrossRef]
72. Bayazit, Ş.S.; Kerkez, Ö. Hexavalent chromium adsorption on superparamagnetic multi-wall carbon nanotubes and activated carbon composites. *Chem. Eng. Res. Des.* **2014**, *92*, 2725–2733. [CrossRef]
73. Zhu, J.; Gu, H.; Guo, J.; Chen, M.; Wei, H.; Luo, Z.; Colorado, H.A.; Yerra, N.; Ding, D.; Ho, T.C.; et al. Mesoporous magnetic carbon nanocomposite fabrics for highly efficient Cr(vi) removal. *J. Mater. Chem. A* **2014**, *2*, 2256–2265. [CrossRef]
74. Zhang, X.; Lv, L.; Qin, Y.; Xu, M.; Jia, X.; Chen, Z. Removal of aqueous Cr(VI) by a magnetic biochar derived from Melia azedarach wood. *Bioresour. Technol.* **2018**, *256*, 1–10. [CrossRef] [PubMed]
75. Zhang, J.; Yang, X.; Shi, J.; Zhao, M.; Yin, W.; Wang, X.; Wang, S.; Zhang, C. Carbon matrix of biochar from biomass modeling components facilitates electron transfer from zero-valent iron to Cr(VI). *Environ. Sci. Pollut. Res.* **2021**, *29*, 24309–24321. [CrossRef] [PubMed]
76. Jung, C.; Heo, J.; Han, J.; Her, N.; Lee, S.-J.; Oh, J.; Ryu, J.; Yoon, Y. Hexavalent chromium removal by various adsorbents: Powdered activated carbon, chitosan, and single/multi-walled carbon nanotubes. *Sep. Purif. Technol.* **2013**, *106*, 63–71. [CrossRef]
77. Yang, J.; Yu, M.; Chen, W. Adsorption of hexavalent chromium from aqueous solution by activated carbon prepared from longan seed: Kinetics, equilibrium and thermodynamics. *J. Ind. Eng. Chem.* **2015**, *21*, 414–422. [CrossRef]
78. Pholosi, A.; Naidoo, E.B.; Ofomaja, A.E. Intraparticle diffusion of Cr(VI) through biomass and magnetite coated biomass: A comparative kinetic and diffusion study. *South Afr. J. Chem. Eng.* **2020**, *32*, 39–55. [CrossRef]
79. Baikousi, M.; Daikopoulos, C.; Georgiou, Y.; Bourlinos, A.; Zbořil, R.; Deligiannakis, Y.; Karakassides, M.A. Novel Ordered Mesoporous Carbon with Innate Functionalities and Superior Heavy Metal Uptake. *J. Phys. Chem. C* **2013**, *117*, 16961–16971. [CrossRef]
80. Ibrahim, M.; Nada, A.; Kamal, D.E. Density functional theory and FTIR spectroscopic study of carboxyl group. *Indian J. Pure Appl. Phys.* **2005**, *43*, 911–917.
81. Fanning, P.E.; Vannice, M.A. A DRIFTS study of the formation of surface groups on carbon by oxidation. *Carbon* **1993**, *31*, 721–730. [CrossRef]
82. Sawalha, M.F.; Peralta-Videa, J.R.; Saupe, G.B.; Dokken, K.M.; Gardea-Torresdey, J.L. Using FTIR to corroborate the identity of functional groups involved in the binding of Cd and Cr to saltbush (Atriplex canescens) biomass. *Chemosphere* **2007**, *66*, 1424–1430. [CrossRef]
83. Nakamoto, K. *Infrared and Raman Spectra of Inorganic and Coordination Compounds*; Wiley: New York, NY, USA, 1997.
84. Gardea-Torresdey, J.L.; Tiemann, K.J.; Armendariz, V.; Bess-Oberto, L.; Chianelli, R.R.; Rios, J.; Parsons, J.G.; Gamez, G. Characterization of Cr(VI) binding and reduction to Cr(III) by the agricultural byproducts of Avena monida (Oat) biomass. *J. Hazard. Mater.* **2000**, *80*, 175–188. [CrossRef]
85. Kong, X.; Han, Z.; Zhang, W.; Song, L.; Li, H. Synthesis of zeolite-supported microscale zero-valent iron for the removal of Cr6+ and Cd2+ from aqueous solution. *J. Environ. Manag.* **2016**, *169*, 84–90. [CrossRef] [PubMed]
86. Greenwood, N.N.; Gibb, T.C. *Mössbauer Spectroscopy*; Chapman & Hall: London, UK, 1971.
87. Cullity, B.D.; Graham, C.D. *Introduction to Magnetic Materials*; John Wiley & Sons: Hoboken, NJ, USA, 2009.